145 (2023) 213263

Contents lists available at ScienceDirect

Biomaterials Advances

journal homepage: www.journals.elsevier.com/materials-science-and-engineering-c

Core-satellite nanoreactors based on cationic photosensitizer modified hollow CuS nanocage for ROS diffusion enhanced phototherapy of hypoxic tumor

Xin Mu [a], Yulei Chang [b], Ying Bao [c], Anni Cui [a], Xiahua Zhong [a], Griffin B. Cooper [c], Anika Guo [c], Guiye Shan [a,*]

[a] Centre for Advanced Optoelectronic Functional Materials Research, Key Laboratory for UV Light-Emitting Materials and Technology of the Ministry of Education, Northeast Normal University, 5268 Renmin Road, Changchun 130024, China
[b] State Key Laboratory of Luminescence and Applications, Changchun Institute of Optics, Fine Mechanics and Physics, Chinese Academy of Sciences, Changchun, 130033, Jilin, China
[c] Department of Chemistry, Western Washington University, Bellingham, WA 98225, USA

ARTICLE INFO

Keywords:
Hollow CuS nanocage
Cationic polymer-modified photosensitizers
ROS diffusion enhanced PDT

ABSTRACT

Photodynamic therapy (PDT) efficiency is directly affected by the reactive oxygen species (ROS) generated by photosensitizers. However, ROSs' ultrashort life span and limited diffusion distance restrict the PDT efficiency. Therefore, it is important to control the delivery strategy of photosensitizers for PDT treatment. Herein, the core-satellite nanoreactors were fabricated with oxygen generation and ROS diffusion properties. The hollow CuS encapsulating horseradish peroxidase (HRP) was combined with the cationic photosensitizers (PEI-Ce6). The unique photosensitizers delivery strategy makes the nanoreactors achieve ROS diffusion-enhanced PDT effect. First, HRP in "core" (HRP@CuS) can decompose hydrogen peroxide (H_2O_2) to O_2, increasing O_2 levels on the surface of the nanoreactor. Second, the Ce6 molecules covalent-linked with PEI are uniformly dispersed on the surface of CuS as a "satellite", avoiding Ce6 aggregation and causing more Ce6 molecules be activated to produce more $^1O_2$. Due to the Ce6 was on the surface of the CuS nanocages, the generated ROS may ensure a larger diffusion range. Meanwhile, the inherently CuS nanocages exhibit photothermal and photoacoustic (PA) effect. The photothermal effect further enhances the ROS diffusion. Under the guidance of PA imaging, nanoreactors exhibit highly efficient hypoxic tumor ablation via photodynamic and photothermal effect. Overall, the core-satellite nanoreactors provide an effective strategy for tumor therapy, further promoting the research of photosensitizers delivery.

1. Introduction

Photodynamic therapy (PDT) has the advantage of being able to deliver precise and effective treatment with minimal side effects, compared to conventional oncology treatment [1,2]. PDT process generally uses photosensitizers to ablate tumor cells by the conversion of oxygen (O_2) molecular into reactive oxygen species (ROS) under laser light irradiation [3,4]. Therefore, the effective contact of photosensitizers with sufficient O_2 is important for O_2-dependent PDT treatment. Generally, the photosensitizers are non-tumor specific and hydrophobic, and low molecular weights (<1000 Da) [5,6]. Many delivery strategies have been developed based on encapsulating photosensitizers in the carrier, such as liposomes, polymeric micelles, etc. However, these carriers hard to achieve the PDT process in tumor effectively due to the aggregation-caused quenching (ACQ) and premature release behavior of photosensitizers. Moreover, ROS itself has short lifespan (<2 ms) and limited diffusion distance inevitably reduces the therapeutic effect [7–9]. The rapid oxygen consumption decreases the PDT effect during the ROS reaction progresses in the hypoxic microenvironment of the tumor [10–12]. Therefore, it is exigent and indispensable to fabricate a unique nanoreactor with an O_2 supply for the stable delivery of photosensitizers as well as enhancing the ROS diffusion.

Recently, different strategies have been developed based on the conversion of tumor-abundant endogenous H_2O_2 to sufficient O_2 for

* Corresponding author.
E-mail address: shangy229@nenu.edu.cn (G. Shan).

https://doi.org/10.1016/j.bioadv.2022.213263
Received 24 September 2022; Received in revised form 8 December 2022; Accepted 16 December 2022
Available online 20 December 2022

hypoxia tumor therapy [13–15]. Therefore, it is important to develop the catalytic decomposition strategy of H_2O_2 to improve tumor hypoxia. Due to the excellent catalytic efficiency and selectivity, natural enzymes have been widely used in the fields of biocatalysts. For example, the horseradish peroxidase (HRP) exhibits the ability to decompose the endogenous H_2O_2 near the mitochondria to O_2 [16–18]. However, the wide applicability of HRP is hindered by the poor stability in physiological environments. Carriers play an important role in improving HRP stability and tumor hypoxia reversion process. The construction of nanocarriers (mesoporous materials, MOFs, etc.) loading HRP is urgent and necessary. Especially the porous structure of the nanoreactor protects the stability of the enzyme while achieving efficient diffusion of H_2O_2 and oxygen within and beyond the skeletons simultaneously [19–21].

The O_2 is converted to ROS by photosensitizer during PDT process. Therefore, the effective contact of photosensitizers with sufficient O_2 is important for O_2-dependent PDT treatment. However, limited physiologic stability of photosensitizer still impedes the application in PDT [22,23]. Many strategies have been developed to deliver non-targeted hydrophobic photosensitizers to the tumor, such as liposomes, polymeric micelles, etc. [24–26]. As the promising photosensitizer, Ce6 has been frequently applied for tumor therapy. However, like most photosensitizers, Ce6 has the drawbacks of limited water solubility, liable to aggregation in physiologic environments, and less accumulation in tumor tissues. A delivery strategy is urgently needed to achieve dispersion of Ce6 and improve the stability in physiological environments. Notably, cationic polymer-modified photosensitizers with specific structures have demonstrated the ability to separate individual photosensitizers and effectively avoid aggregation [27–29], thereby remarkably enhancing the conversion efficiency and diffusion range of ROS. The cationic polymer polyethylenimine (PEI) is a very distinctive water-soluble polymer. The primary, secondary, and tertiary amines contained in the molecule endow PEI with excellent chemical reactivity and internalization capability [30,31]. The combination of PEI and Ce6 by covalent bond enables efficient Ce6 dispersion and cellular accumulation. Thus, the above strategy hopefully improves the availability of Ce6 in PDT process.

CuS particles show strong potential in tumor therapy owing to the powerful absorbance in the NIR area, high photothermal conversion effectiveness (PCE), low cytotoxicity, and photoacoustic imaging capability [32–34]. In particular, the previously reported template sacrificial method allows the CuS be constructed into hollow mesoporous structure [35], which provides a channel for the O_2. However, the combination of cationic polymer modified photosensitizer and hollow CuS are infrequently utilized in the treatment of hypoxic tumors.

Considering the above problems, we fabricated core-satellite nanoreactors based on hollow CuS nanocage and PEI-Ce6, further encapsulate HRP to obtain O_2 self-supply for hypoxic tumor phototherapy. As shown in Scheme 1, after tail vein injection, hyaluronic acid (HA) active targets the overexpressed CD44 on the surface of tumor cells. The nanoreactors with specific sizes (~120 nm) ensure the enhancement of internalization through passive targeting. Furthermore, the HRP catalyzes the conversion of H_2O_2 to O_2 within tumor cells, effectively enhancing the abundance of O_2. At the same time, the photothermal effect of CuS offers the possibility of PTT and PA imaging. PEI-Ce6, the cationic polymer modified photosensitizer, is connected on the surface of the O_2-riched "core" (HRP@CuS) by thiol group. This "satellite" architecture avoids unnecessary quenching of PS and improves the ROS

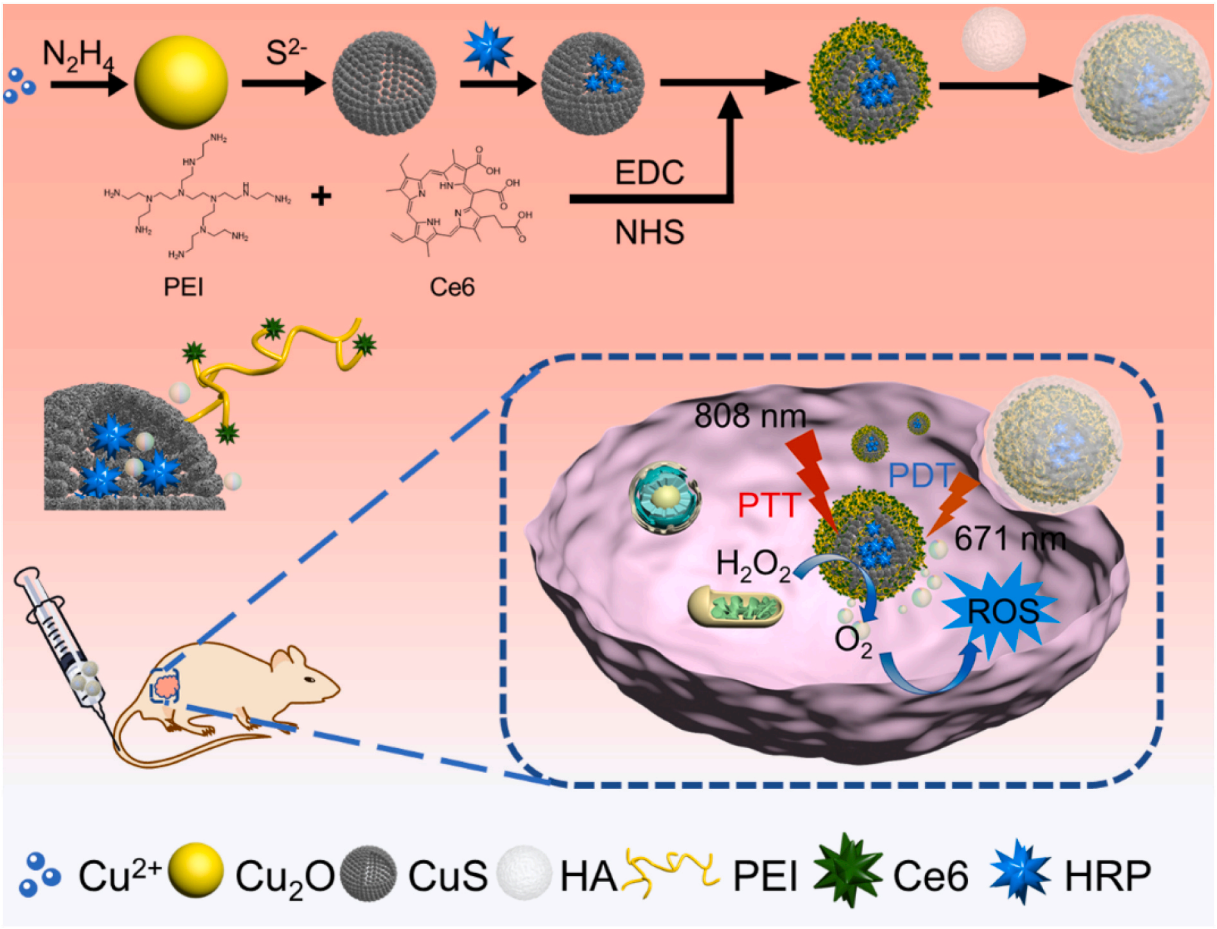

Scheme 1. A scheme showing the preparation and application of HRP@CuS-PEI-Ce6@HA.

production. Above all, ROS is generated on the surface instead of the core of the nanoreactors, ensuring a larger diffusion range as the temperature rises. Stimulated by external near-infrared light, this unique nanoreactor (HRP@CuS-PEI-Ce6@HA, abbreviated as HRP@CPC@HA) enables efficient phototherapy with precise guidance of PA imaging for superb hypoxic tumor ablation.

2. Experimental section

2.1. Materials

Copper chloride dihydrate ($CuCl_2{\cdot}2H_2O$) was obtained by Tianjin Guangfu Chemical Agent Co., Ltd. (Tianjin, China). Vinyl pyrrolidone polymer (PVP K30), sodium hydroxide (NaOH), hydrazinium hydroxide solution ($N_2H_4{\cdot}H_2O$), acetothioamide (CH_3CSNH_2), carbodiimide hydrochL (EDC·HCl), thiazolyl blue (MTT) and dimethyl sulfoxide (DMSO) were bought from Aladdin Reagent (Shanghai, China). Polyethylenimine (PEI), acid hyaluronic (HA), mercaptopropionic acid, tris (4,7-biphenyl-1,10-phenanthroline) ruthenium dichloride (RDPP) and Ce6 was obtained from J&K Scientific. (Beijing, China). DCFH-DA was obtained from Sigma-Aldrich. Roswell Park Memorial Institute-1640 (RPMI-1640) culture medium, fetal bovine serum (FBS), Dulbecco's phosphate buffered saline (PBS), trypsin, and penicillin−streptomycin were obtained from Invitrogen Corp.

2.2. Preparation of HRP@CPC@HA

All the following experiments were performed in triplicate unless specifically mentioned.

Hollow CuS nanoparticles were prepared by the previously reported sacrifice template method [35]. 0.3 g PVP was dissolved in 30 mL of deionized water, 2 mmol/L $CuSO_4$ was added into the PVP solution with magnetic stirring for 1 h. 25 mL of fresh NaOH solution was then added to adjust the pH value to 9. After stirring for 2 min, $N_2H_4{\cdot}H_2O$ (2.0 mL, 0.10 mol/L) was added and reacted for 8 min to obtain Cu_2O. Acetothioamide (0.266 mmol, final molarity) was infused to the Cu_2O and reacted at 40 °C for 2 h to obtain the hollow CuS. The obtained hollow CuS was then rinsed with distilled water and collected by centrifuging at 8000 rpm for 5 min before being vacuum dried.

The HRP and CuS (weight ratio, 1:1) were mixed with distilled water and sonicated for 30 min, then stirred overnight and collected via centrifuge at 8000 rpm for 5 min. The precipitate was washed with distilled water and dried at 25 °C under vacuum to obtain HRP@CuS. The product of the previous step was dispersed in deionized water with mercaptopropionic acid (weight ratio, 1:1) and stirred slowly overnight. The precipitate was collected by centrifuging at 8000 rpm for 5 min, then washed 3 times with deionized water to obtain HRP@CuS-COOH. HRP@CuS-PEI was prepared as described below. Briefly, excess EDC and NHS were dispersed in DMSO, HRP@CuS-COOH was slowly added and stirred at room temperature for 3 h to complete the activation of the carboxyl groups. Then a solution of DMSO and PEI (1 mg/mL) was added drop by drop and stirred overnight. The next day the whole system was transferred to a 2000 Da dialysis bag for 72 h against water to remove unreacted chemicals and organic solvents. HRP@CPC is also prepared using a similar EDC/NHS method; the reaction and dialysis process needs to be carried out in the dark. Finally, the complexation of HRP@CPC and HA was formed by mixing HRP@CPC and HA (mass ratio 1:0.6) in deionized water. After stirring overnight, the precipitate was collected by centrifugation at 8000 rpm for 5 min and stored in PBS at −4 °C.

HS-PEI and HS-PEI-Ce6 were obtained by using a similar EDC/NHS method without the CuS nanocages. The weight ratio of PEI and mercaptopropionic acid was 15:1, and the weight ratio of HS-PEI and Ce6 was 5:1.

2.3. Singlet oxygen production by HRP@CPC@HA

1,3-Diphenylisobenzofuran (DPBF) was chosen as a detector to measure the production of singlet oxygen in HRP@CPC@HA nanoreactors under 671 nm irradiation, as DPBF is susceptible to oxidation by ROS to alter its structure, resulting in a sluggish decrease in its peak value of absorption (410 nm). In a representative procedure, 50 μL of DPBF (1 mg/mL, ethanol solution) was infused with the HRP@CPC@HA solution. UV–visible absorption spectra of DPBF were recorded and contrasted over time under the 671 nm laser irradiation (10 mW/cm^2).

The ROS content in cells was measured using 2,7-dichlorodihydrofluorescein diacetate (DCFH-DA) as a probe of ROS. The DCFH-DA is oxidized by intracellular ROS and emits a vivid green fluorescence, thus showing the ROS content in cells. 4T1 cells purchased from the CAS cell bank were incubated with HRP@CPC@HA dispersion (50 μg/mL) at 37 °C for 12 h. After, the cells were washed with PBS. Then 10 μM DCFH-DA was infused and incubated for 30 min. Cells were then washed 3 times with PBS to take out the extracellular indicators. Finally, the cells were irradiated with a 671 nm (0.15 W/cm^2) laser for 10 min and then observed on a confocal fluorescence microscope.

2.4. Cellular uptake

Pre-treated coverslips were UV irradiated, dried, and laid on the bottom of 6-well plates. Digest 4T1 cells to form a cell suspension, migrate into 6-well plates and control the number of cells per well to approximately 2.0×10^5. After 24 h of incubation, the medium was taken out and a concentration of HRP@CPC@HA dispersion or the same amount of free Ce6 was infused. After 24 h, the cells were washed 3 times with PBS to take out extracellular nanomaterials or photosensitizers Finally, the cells were fixated with 3.7 % paraformaldehyde (POM) for 15 min at 20 °C and washed 4 times carefully with PBS. Afterwards, 1 μL of DAPI (1 mg/mL) was infused to each well at 37 °C for 15 min to stain the nuclei, then washed again three to five times with PBS. The coverslips are gently taken out and set on a slide with glycerol, shaded for 10 min, sealed, and stored at 4 °C. The cells were observed and the uptake of the dye was detected by laser confocal microscopy.

2.5. Cytotoxicity and enhanced PDT in cells of HRP@CPC@HA

Thiazolyl blue (MTT) reagent was chosen to examine the cytotoxicity of HRP@CPC@HA. 4T1 cells were diverted into 96-well plates and cultured for 24 h. Then the HRP@CPC@HA dispersion with different concentrations (i.e., 0, 50, 75, 100, 150, 300 ppm) was infused and incubated at 37 °C for 24 h. Subsequently, 10 μL of MTT (5 mg/mL) was added to each well of the 96-well plate and co-incubated at 37 °C for 4 h. Finally, remove the liquid from each well, and 150 μL of DMSO was infused to each well, then carefully shake the plate at 25 °C for 20 min. The relative viability of the cells was recorded and the cytotoxicity of each group was calculated by monitoring the absorbance of MTT.

4T1 cells were diverted into a 96-well plate and incubated for 24 h (5 % CO_2, 37 °C). Then, the RPMI 1640 medium containing different concentrations of materials were infused for 12 h. After the cells were washed 3 times with PBS to take out excess materials, the cells were irradiated (671 nm laser, 0.15 W/cm^2 or 808 nm laser, 0.15 W/cm^2). Then, the cells were delivered to a fresh medium for 12 h and the cell viability was calculated by typical MTT assay.

2.6. Live/dead cell staining test

The cells were cultured for 12 h in a 6-well plate, then treated with CuS, PC, CPC, or HRP@CPC. After 4 h, the treated cells were irradiated by laser (0.2 W/cm^2, 3 min). The treated cells were co-stained with Calcein AM (2 μM) and PI (4 μM) following the protocol of Live/Dead viability/cytotoxicity kit before an examination by confocal laser scanning microscopy (CLSM).

2.7. Blood circulation and biodistribution of HRP@CPC@HA

Female Balb/c mice (weight ≈20 g) were obtained from Beijing Charles River Laboratory Animal Technology Co., Ltd. All animal experiments were treated in line with the animal experiments ethical committee for caring. We chose the 4T1 cell line as the mouse breast cancer subcutaneous tumor model. After the cells were cultured to a certain amount, the cells were digested by trypsin and washed 3 times using PBS before being redispersed in PBS with a concentration of 1.0×10^7/mL. A 50 μL cell dispersion was inoculated subcutaneously in the right hind leg of each mouse body, and about two weeks later, the mice were used for the following experiments.

The female Balb/c mice were injected intravenously with HRP@CPC@HA ($n = 3$), and 20 μL blood was collected at different time points (5 min, 10 min, 20 min, 40 min, 60 min, 120 min, 480 min, and 1440 min). The content of Cu in the blood samples was measured by ICP-AES. The pharmacokinetic model was chosen to calculate the blood half-life of HRP@CPC@HA.

4T1 tumor-bearing mice were chosen as the animal model to perform the biodistribution of HRP@CPC@HA ($n = 3$). Mice were sacrificed at different time points (4-12 h) after intravenous injection (200 μL of HRP@CPC@HA, [Cu] = 10 mg/kg in PBS). The major organs (heart, liver, spleen, lung, and kidney) and tumor were harvested, weighed, and homogenized. HRP@CPC@HA in various organs and tumor was expressed as a percentage of the injected dose per gram of tissue (%ID/g).

2.8. Tumor treatment

Thirty 4T1 tumor bearing mice were picked out and divided into 6 groups **i)** PBS, **ii)** Ce6 + 671 nm, **iii)** HRP@CuS-Ce6@HA + 671 nm, **iv)** HRP@CPC@HA + 671 nm, **v)** CPC@HA + 808 nm + 671 nm and **vi)** HRP@CPC@HA + 808 nm + 671 nm). After the intravenous injection for 24 h (200 μl of HRP@CPC@HA, [Cu] = 10 mg/kg in PBS), the mice were treated according to Fig. 7a. The tumor volume was calculated every 2 days as length × $(\text{width})^2 \times 1/2$. The relative tumor volume was calculated as V/V_0, where V_0 and V represent the tumor volume on the first day and on the day of measurement.

2.9. Organ tissue H&E staining

To evaluate the safety of the nanoreactor treatment, pathological analysis of the major organs (heart, liver, spleen, lung, and kidney) was performed. The dissected fresh organs were washed with PBS and soaked in 4 % paraformaldehyde. The organs were sealed by paraffin embedding. Each tissue was cut into 5 μm sections and treated with Hematoxylin and Eosin (H&E) staining was performed, and H&E-stained sections were photographed and pathologically analyzed with a fluorescence microscope.

3. Results and discussion

3.1. Synthesis and characterization of HRP@CPC@HA

The synthetic route for the fabrication of CuS-PEI-Ce6 is present in Scheme 2. Cu_2O nanoparticles were firstly obtained by a solvothermal approach. Then, hollow CuS may be formed based on the sulfidation with acetothioamide. Fig. 1a shows the transmission electron microscope (TEM) image of CuS. The prepared CuS was monodisperse with an overall diameter of ≈100 nm. The dark edge and the pale center demonstrate the hollow structure. After being coated with HA, the TEM image shows a transparent layer on the surface of CuS (Fig. 1b). As shown in Fig. 1c, the hydrodynamic diameter of CuS nanocages is about 100 nm. The HRP@CuS shows similar size with CuS nanocages. This suggests the HRP was encapsulated by CuS. After surface modification of PEI-Ce6 (abbreviated as PC) and coating of HA, the particle size increases to 160 nm. The crystalline structure of the synthesized hollow CuS nanocage was identified by using powder X-Ray diffraction (XRD) (Fig. 1d). The characteristic peaks appear at $2\theta = 29.3$, 31.7, 47.9 and 59.3°, corresponding well to (102), (103), (110), and (116) crystal planes of the hexagonal covellite structure (JCPD file No. 06-0464). To demonstrate the covalent linkage between Ce6 and PEI, the FTIR spectrum spectra of HS-PEI and HS-PEI-Ce6 were measured (Fig. 1e). Characteristic peaks of the amide bond were measured in the PEI-Ce6 spectrum, the peak at 1660 cm^{-1} (C═O) and 1410 cm^{-1} (C—N) are attributed to the stretching vibration of the amide bond, distinguishing it from unreacted PEI. The ^1H NMR spectrum further reveals the above conclusions (Fig. 1f). Compared with unreacted PEI and Ce6, the characteristic peaks of Ce6 appeared in the ^1H NMR spectrum of PEI-Ce6 (1.19 ppm, 1.85 ppm, 3.25 ppm). Simultaneously, the peaks of Ce6 appeared at 1.67 ppm, 1.66 ppm, 3.28 ppm respectively. The change of chemical shift confirmed that the chemical reaction between Ce6 and PEI occurred due to the formation of amide bonds. The ultraviolet–visible (UV–vis) absorption spectra were performed to further explain the fabrication of the HRP@CPC@HA. HRP exhibits the absorbance at 410 nm (Fig. 1g), while spectrum of HRP@CuS shows almost no

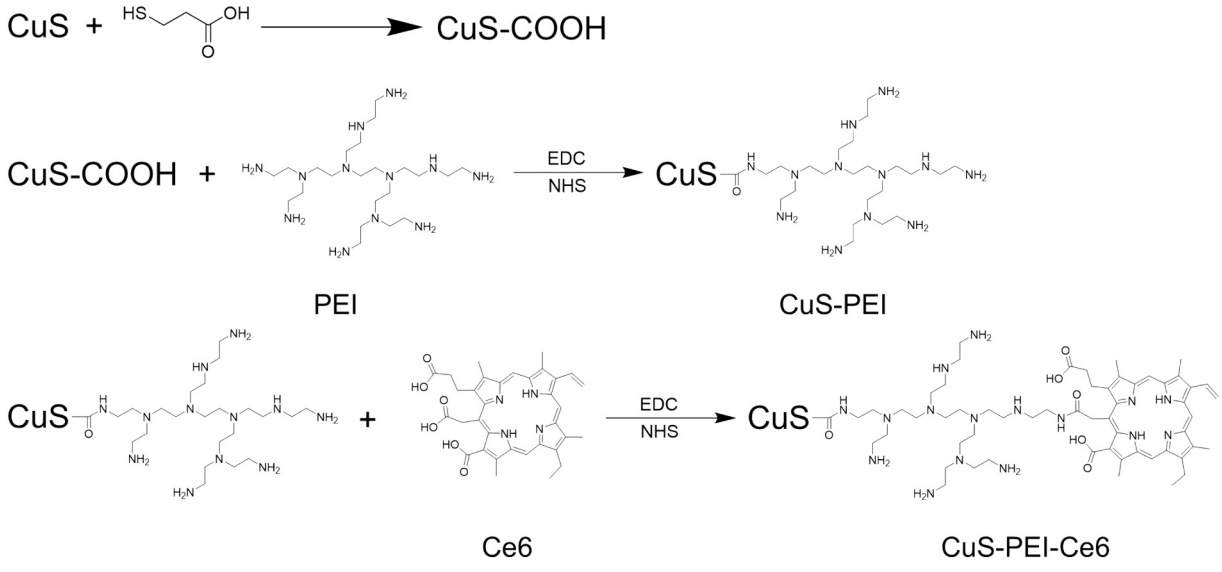

Scheme 2. The synthetic route of CuS-PEI-Ce6.

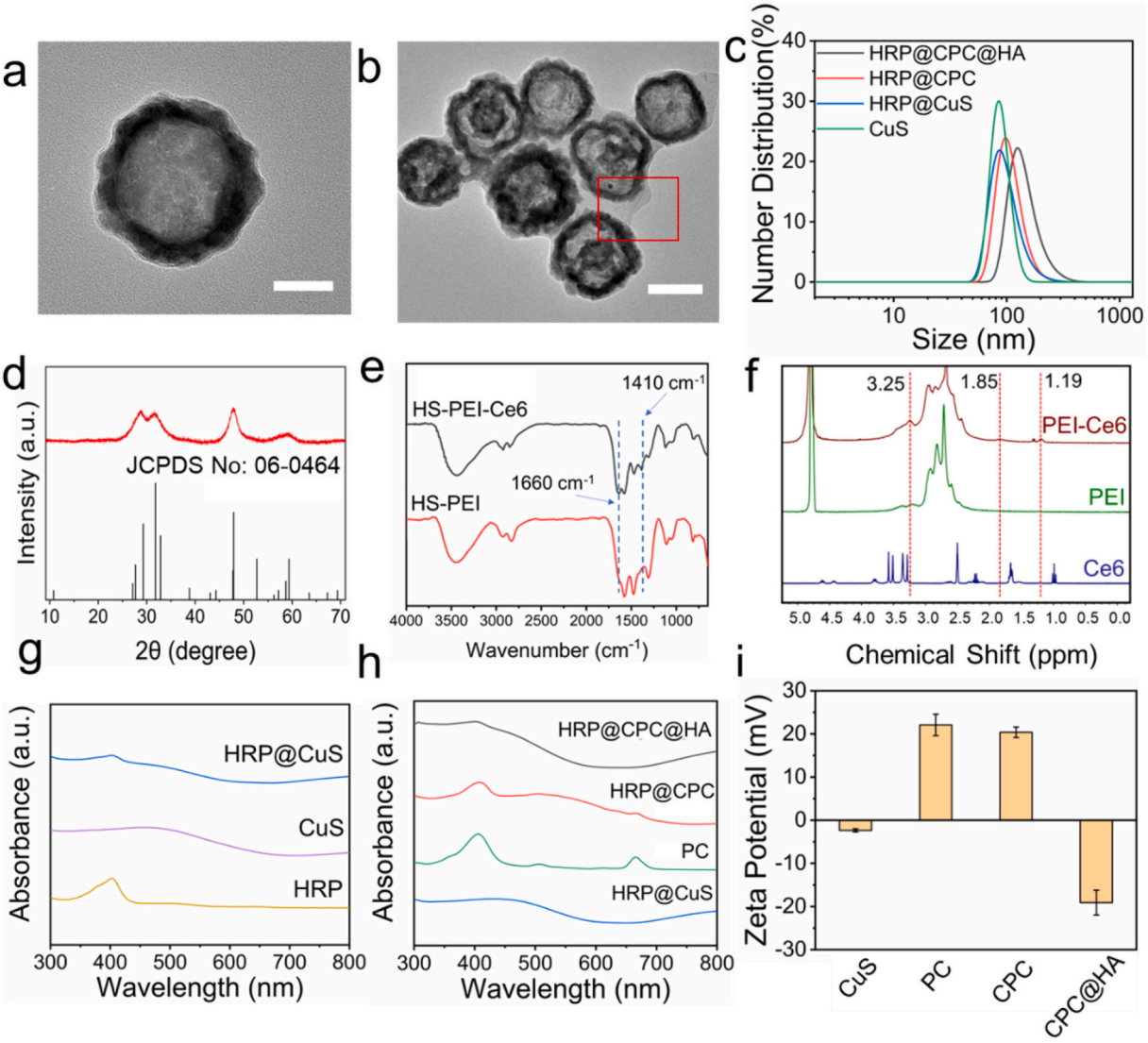

Fig. 1. Transmission electron microscope (TEM) images of **(a)** hollow CuS nanocage (scale bars: 50 nm), **(b)** HRP@CuS-PEI-Ce6@HA (scale bars: 100 nm), **(c)** size distribution of CuS, HRP@CuS, HRP@CuS-PEI-Ce6 and HRP@CuS-PEI-Ce6@HA. **(d)** X-ray diffractograms of hollow CuS. **(e)** The FTIR spectra of HS-PEI-Ce6 and HS-PEI. **(f)** The ^{1}H NMR of Ce6, PEI and PEI-Ce6. **(g)** Absorption spectra of HRP, CuS, and HRP@CuS. **(h)** Absorption spectra of PEI-Ce6, HRP@CuS, HRP@CuS-PEI-Ce6, and HRP@CuS-PEI-Ce6@HA. **(i)** Zeta Potential of CuS, PEI-Ce6, CuS-PEI-Ce6, and CuS-PEI-Ce6@HA.

absorbance at 410 nm. This indicates the HRP was largely encapsulated by CuS. As shown in Fig. 1h, HRP@CPC@HA does not show an obvious absorption peak. In sharp contrast, HRP@CPC exhibits a narrow absorbance at 670 nm, similar to the characteristic absorption peak of Ce6. This suggests that the Ce6 was on the surface of the nanoreactor and HRP@CPC was encapsulated by HA. Fig. 1i shows the zeta potential

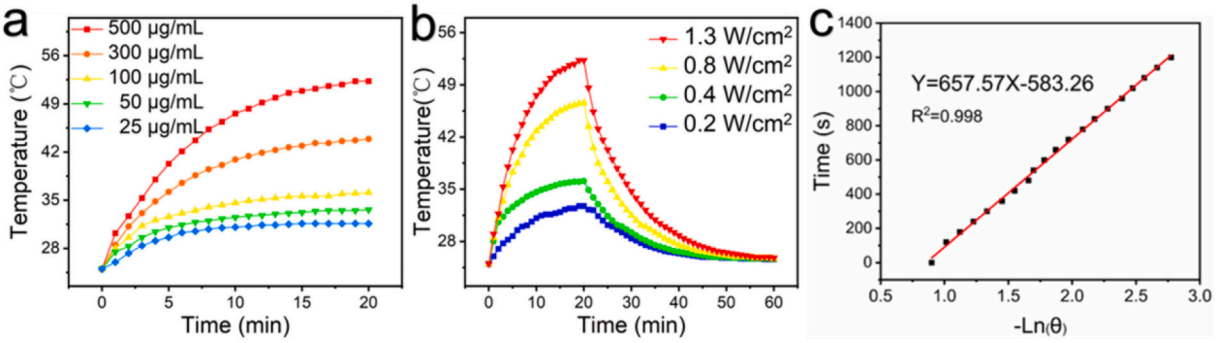

Fig. 2. **(a)** Photothermal heating curves of CuS-PEI-Ce6 at different concentrations with the same power density of 1 W/cm^2 (25–500 μg/mL). **(b)** Photothermal elevating curves of 500 μg/mL CuS-PEI-Ce6 solution with different power densities (0.2–1.3 W/cm^2). **(c)** Plot of time vs. -ln(θ) [θ is the driving-force temperature] from the data measured during the cooling period shown in Fig. 2b.

of CPC is positive (ca. +20.4 mV), demonstrating the cell internalization ability of the CPC. Antithetical, the ζ-potential of CPC@HA in an aqueous solution was negative (ca. −18.7 mV), ensuring the blood circulation capacity of the CPC@HA. The above results indicate HRP@CPC@HA was successfully synthesized and the nanoreactors were fabricated with a core-satellite structure.

3.2. Photothermal process of CPC

The photothermal ability of the obtained CPC with the 808 nm laser irradiation was measured. As shown in Fig. 2a, the photothermal effect could increase monotonically with CPC concentration (25–500 μg/mL). The temperature elevation and reduction curves at different power densities (0.2–1.3 W/cm^2) were shown in Fig. 2b. The temperature elevates to 32.4 °C at a power intensity of 0.2 W/cm^2 irradiation, while the temperature elevation increased to 53.7 °C at 1.3 W/cm^2. The above results indicate that CPC could generate heat efficiently, even under a low power intensity irradiation. Obviously, the temperature could increase monotonically with the content of CPC and irradiation power density. As shown in Fig. 2c, according to the heating-cooling curve (1.3 W/cm^2) and interrelated time constant, the photothermal conversion efficiency (η) of CPC was calculated (ca. 34.91 %). The above results reveal that the CPC produces significant local heat at 808 nm irradiation. This proves that CPC exhibits promising photothermal effect.

3.3. The O_2 generation and enhanced ROS process of HRP@CPC

The O_2 content in the tumor microenvironment is essential for PDT. However, the O_2 content is extremely limited in the hypoxic tumor. Fortunately, the endogenous H_2O_2 could be decomposed by HRP, further increasing the O_2 level in tumor cells. Therefore, the O_2 generation capability of HRP@CPC was determined via a portable dissolved oxygen meter. Fig. 3a shows the O_2 concentration gradually increased with time after adding HRP@CPC to the H_2O_2 solution. Almost no O_2 generation occurred in HRP@CPC group, CPC + H_2O_2 group, and CPC group. The above results reveal that the nanoreactor supplies O_2 efficiently based on the decomposition of H_2O_2 by HRP. The O_2 molecules are converted to ROS by photosensitizer during PDT process. Moreover, the efficiency of PDT is largely limited to the diffusion capacity of generated ROS. To detect the generation of ROS during PDT process, 2,2,6,6-tetramethylpiperidine (TEMP) was chosen as a probe for capturing ROS. The electron spin-resonance (ESR) spectra were measured to determine the species of ROS, as shown in Fig. 3b. Compared to the control group (H_2O), three signal peaks appear in the ESR spectra of PC, Ce6 with an area ratio of 1:1:1, suggesting the generation of $^1O_2$ under laser excitation. Furthermore, the DPBF was used to further characterize the $^1O_2$ production ability of CPC. The change in the absorption peak of the DPBF was examined at 410 nm by UV–Vis absorption spectroscopy (Fig. 3c–e). The absorption shows ignorable decrease for H_2O group. However, for Ce6 and CPC groups, the absorption peaks of DPBF were decreased. This indicates DPBF was oxidized by the generated $^1O_2$. Furthermore, compared with the Ce6 group, the CPC group shows more obviously reduction in the absorption, indicating that more $^1O_2$ generated. This is due to the fact that PEI can separate Ce6, preventing aggregation. These results reveal that the unique structure (O_2-riched core and photosensitizer-suspended satellite) of our nanoreactor leads to O_2 generation and ROS diffusion augment, thereby enhancing of PDT.

3.4. Cytotoxicity and cellular uptake of HRP@CPC@HA

The 4T1 cell line was chosen as the treatment model and the cytotoxicity of the samples was assessed using the MTT method, as shown in Fig. 4a. The cells were treated with PC group, HRP@CuS group and HRP@CPC group respectively. Each group shows negligible cytotoxicity. Notably, the cell viability of HRP@CPC group was over 80 % even at a concentration of 300 μg/mL. The results showed that HRP@CPC was biosafe and biocompatible. The internalization capacity of the CPC directly affects the therapeutic effect of PDT. According to the zeta potential results (Fig. 1i), the internalization ability of CPC was investigated. Photographs were taken using CLSM to verify the cellular uptake of the samples, shown in Fig. 4b. PBS, Ce6, PC and CPC were added

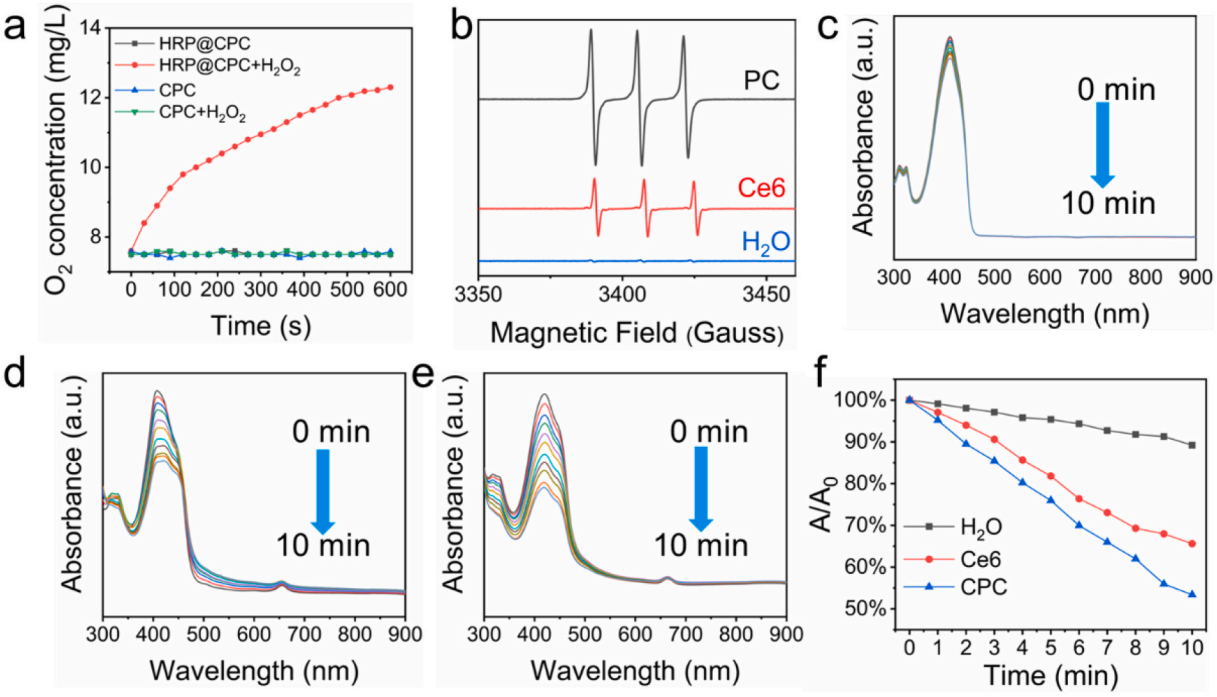

Fig. 3. **(a)** O_2 generation curve of CuS-PEI-Ce6 and HRP@CuS-PEI-Ce6 without and with H_2O_2 addition (100 mM). **(b)** ESR spectra of PEI-Ce6, Ce6 and H_2O after 671 nm laser irradiation (200 mW/cm^2, 10 min) in the presence of TEMP. Decay curves of DPBF absorption in **(c)** H_2O, **(d)** Ce6 or **(e)** CuS-PEI-Ce6 solution after different time of irradiation (671 nm, 10 mW/cm^2). **(f)** Variation of absorption peak at 410 nm with different time in Fig. 3c-e.

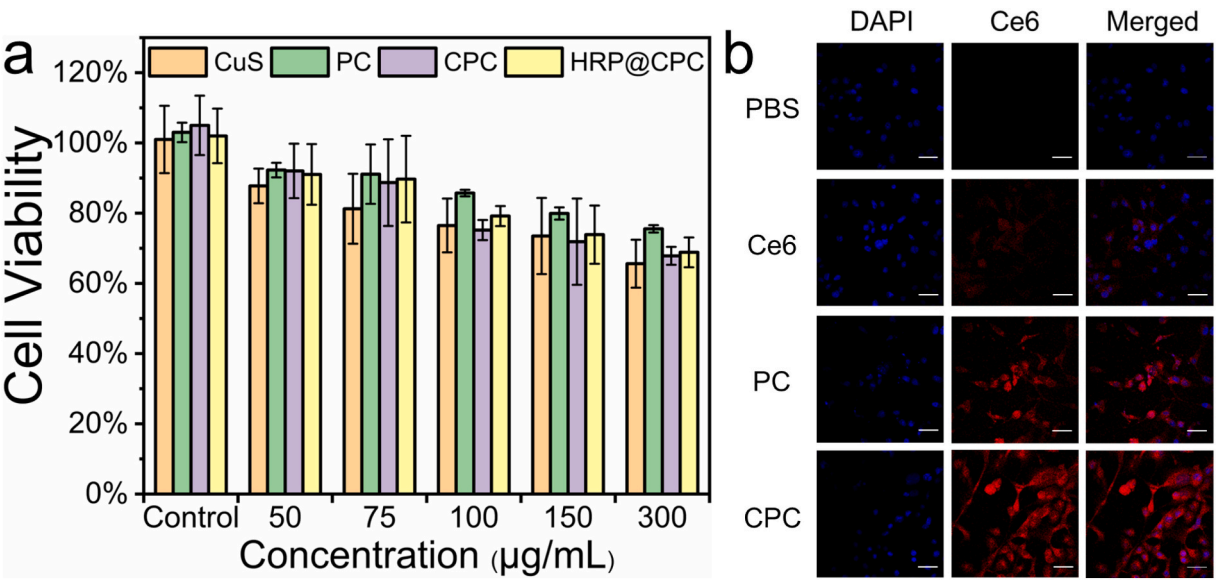

Fig. 4. **(a)** Cytotoxicity assays of 4T1 cells incubated with CuS, PEI-Ce6, CuS-PEI-Ce6 and HRP@CuS-PEI-Ce6 for 24 h. **(b)** CLSM images of 4T1 cells pre-incubated with free Ce6, PEI-Ce6, CuS-PEI-Ce6 for 24 h. Scale bars: 50 μm.

respectively and then co-incubated with 4T1 cells for 4 h. The location of the cells was verified using DAPI staining of the nuclei (blue) and the fluorescence of Ce6 itself (red) was used to determine the intracellular content to verify the internalization of each group. PBS was used as a control group. The fluorescence intensity in each photo depends on the Ce6 concentration, so the PBS group shows no red fluorescence. For the free Ce6 group, the hydrophobic aggregation of Ce6 in the culture leads to quenching of the fluorescence. Compared with Ce6 group, PC group shows obviously red fluorescence. This is due to the covalent linkage between Ce6 and PEI allows Ce6 to be stably dispersed, avoiding quenching due to aggregation. Moreover, the interaction between positive PC and negative-charged cell membrane further enhancing the internalization of PC. CPC group exhibits the greatest fluorescence brightness. Combining large-sized CuS and positively charged PEI promotes the internalization of Ce6, thereby CPC exhibits the greatest internalization ability. The above results reveal that our nanoreactor has low cytotoxicity and excellent internalization capability.

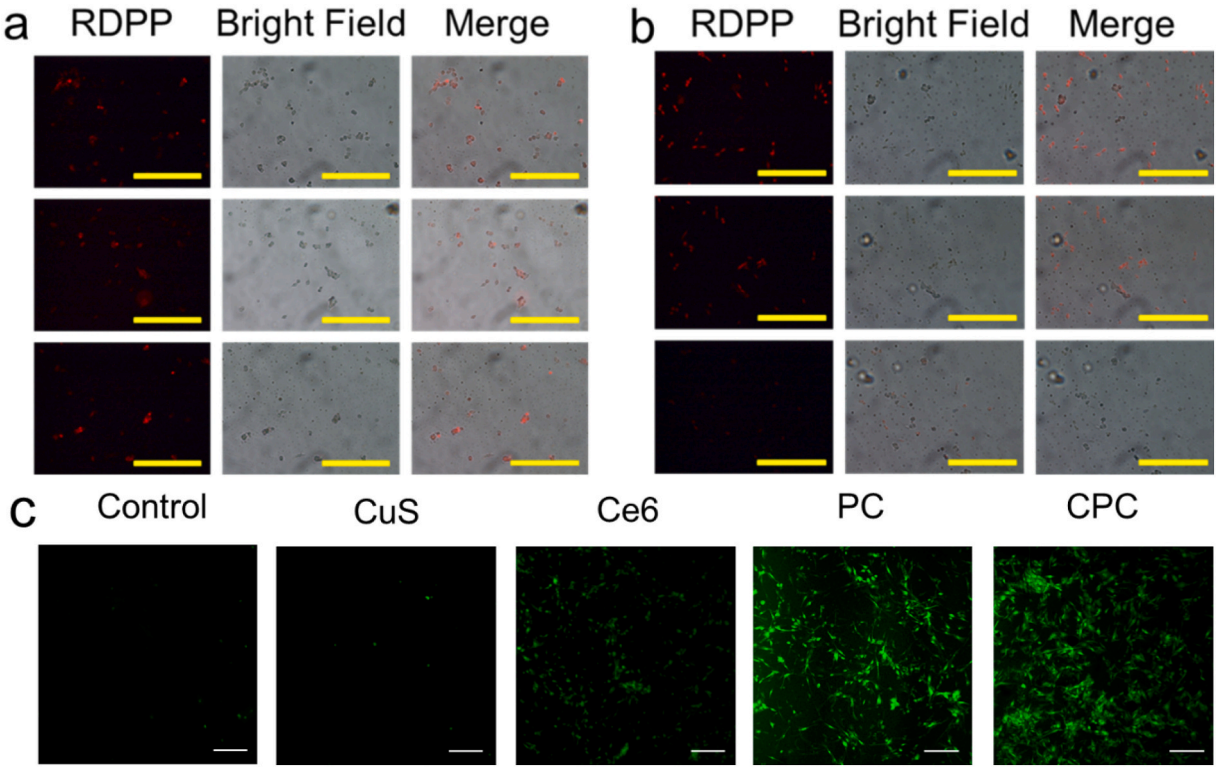

Fig. 5. Fluorescence images of 4T1 cells incubated with RDPP and then treated with **(a)** PBS or **(b)** HRP@CuS-PEI-Ce6 for different times (top to bottom). Scale bars: 500 μm. **(c)** CLSM images of 4T1 cells cultured with DCFH-DA and then treated with PBS (control), Ce6, CuS, PEI-Ce6, CuS-PEI-Ce6 respectively for 24 h then irradiated with a power density of 0.2 W/cm^2 for 3 min. Scale bar = 100 μm.

3.5. Intracellular O_2 and ROS generation

RDPP was chosen as the intracellular O_2 probe. The O_2 generation capacity of HRP@CPC was verified by fluorescence images, as shown in Figure 5a-b. 4T1 cells were pre-incubated with RDPP for 24 h, then incubated with HRP@CPC for 30 min. 4T1 cells were observed by a fluorescence microscope. The red fluorescence of RDPP was strongly reduced in Fig. 5b. This indicates the O_2 generation capability of HRP@CPC. Comparatively, the fluorescence intensity of the PBS group shows insignificant change. The above results reveal that HRP@CPC could generate O_2 effectively in the hypoxic tumor cells.

The ROS content in the tumor cells is also essential for PDT process. DCFH-DA was chosen as the ROS probe to measure the content of ROS. The ROS production capacity was examined by CLSM photographs, as shown in Fig. 5c. 4T1 cells were pre-incubated with each group of material for 24 h, then DCFH-DA was added and incubated for 30 min. Subsequently, the petri dish was irradiated by 671 nm laser, and the resulted image was recorded by CLSM. The image shows almost no green spots appear in the control group and CuS group. The image of the Ce6 treatment group shows the weaker fluorescence intensity. This reveals few ROS was generated after treated with Ce6. This is due to the aggregation of free Ce6. The obviously fluorescence signals for PC and CPC groups are evidence of significant ROS generation. The generated ROS level depends on the CuS and PEI guided effective separation of Ce6, further enhancing the diffusion of ROS. The genuine results are also in treaty with internalization (Fig. 4b). The above findings suggest that the CPC sample ensures the enhancement of ROS diffusion.

3.6. Enhanced PDT by HRP@CPC in vitro

The 4T1 cell was selected as a treatment model for PDT investigation. The cell viability was discovered by MTT analysis, as shown in Fig. 6a. 4T1 cells were pre-incubated with CuS, PC, and CPC for 24 h, then the cells were irradiated using a laser at the wavelength of 808 nm and 671 nm, respectively. Meanwhile, the cell viability of the Ce6 + 671 nm group decreased by 35 %, which was due to the PDT effect. Notably, the cell viability of the HRP@CPC group was only 10 % under the 808 nm and 671 nm irradiation, revealing the photothermal and ROS diffusion-enhanced PDT process. The CuS, CPC, and HRP@CPC groups exhibit decrease in cell viability after the 808 nm irradiation. This reveals that the photothermal effects of CuS are effective in increasing the temperature of cells that leads to partial tumor cell apoptosis. The tumor ablation of HRP@CPC in vitro was also examined by the Live/Dead Staining. As shown in Fig. 6b, the red fluorescence indicates dead cells, while the green fluorescence suggests living cells. As expected, HRP@CPC group exhibits tumor ablation effect, almost all cells show red fluorescence in HRP@CPC group. This is due to the photothermal and ROS diffusion enhanced PDT effect. Conversely, PC group exhibit partial cell apoptosis, which is caused by normal PDT. The above results reveal that HRP@CPC is a unique nanoreactor for efficient tumor suppression via ROS diffusion-enhanced PDT.

3.7. Antitumor effect by HRP@CPC@HA in vivo

The 4T1 tumor model was built for the in vivo anti-tumor investigation of HRP@CPC@HA. The specific treatment protocol was shown in Fig. 7a. 4T1 cells were 14 days post subcutaneous inoculation right posterior side of each mouse body and the size of tumor can reach 100 mm^3 for the following experiments. To evaluate whether HRP@CPC@HA is suitable for antitumor application in vivo, the pharmacokinetics of HRP@CPC@HA was further evaluated by detecting the [Cu] content in blood using ICP-AES (Fig. 7b). After 24-h postinjection, 18.7 μg/ml of [Cu] was determined in the peripheral circulating blood, suggesting considerably long blood retention of HRP@CPC@HA after intravenous injection. Moreover, the blood-circulation half-time of HRP@CPC@HA in the bloodstream was calculated to be 28 min. To evaluate the possible major organs (heart, kidney, lung, spleen, and liver) and tumor distribution of nanoreactor, the biodistribution of HRP@CPC@HA administered by intravenous injection at various time points were obtained. As shown in Fig. 7c, nanoreactor enrichment in the liver at 4–8 h, decreased rapidly over time. HRP@CPC@HA reached a maximum amount (~23 % ID/g) at tumor tissues due to enhanced penetration and retention (EPR) effect after about 24 h of intravenous injection. The typical tumor-specific accumulation of nanoreactor was attributed to the active-targeting tumor pathway of HA. The photoacoustic images of 4T1 tumor-bearing mice were obtained after tail vein injection of HRP@CPC@HA (Fig. 7d). In agreement with the biodistribution results, the PA signal appeared at 4 h (red area), and the

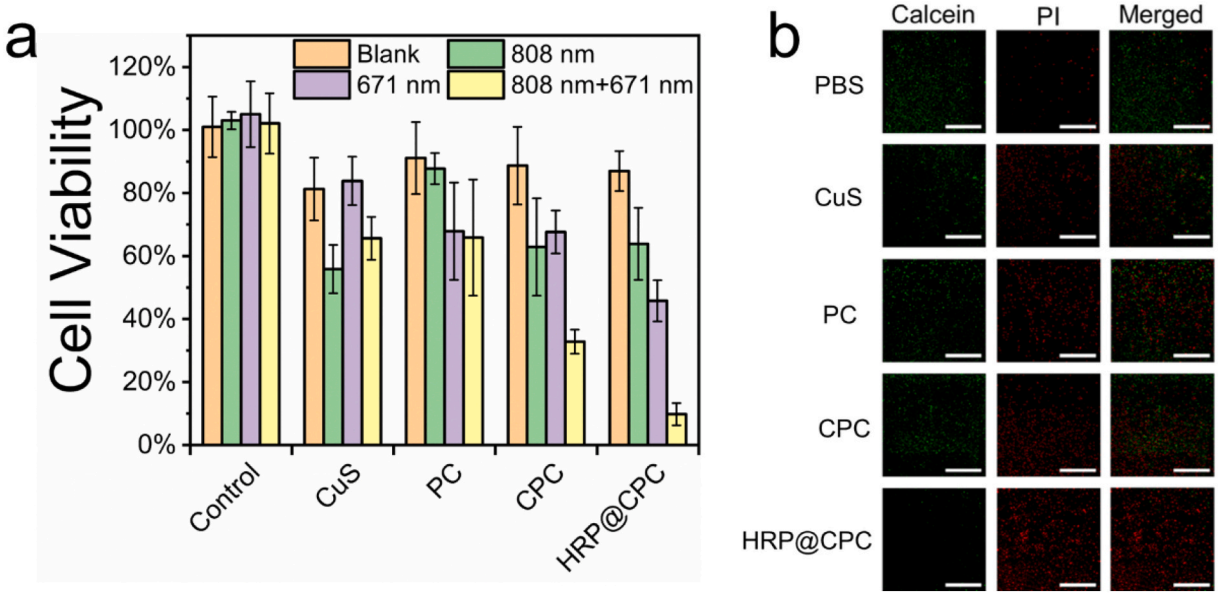

Fig. 6. **(a)** Cell viability of 4T1 cells pre-incubated with CuS, PEI-Ce6, CuS-PEI-Ce6, HRP@CuS-PEI-Ce6, then irradiated with a power density of 0.3 W/cm^2 for 5 min (671 nm or 808 nm). **(b)** CLSM image of 4T1 cells cultured with CuS, PEI-Ce6, CuS-PEI-Ce6, and HRP@CuS-PEI-Ce6 for 24 h then irradiated with a power density of 0.2 W/cm^2 for 3 min. Scale bar = 500 μm.

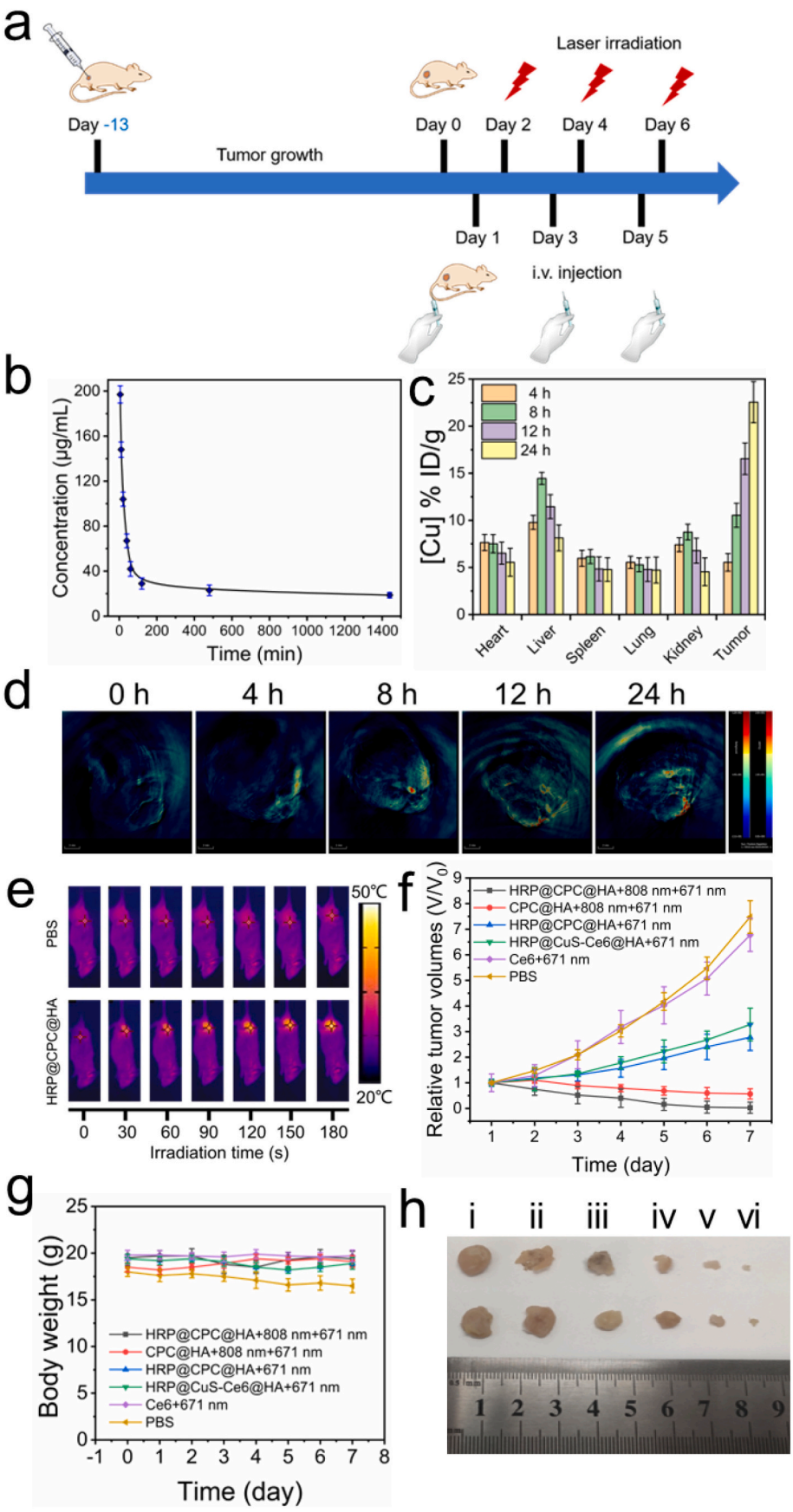

Fig. 7. **(a)** A scheme showing the 4T1 tumor-bearing mice treatment protocol. **(b)** The blood-circulation curve of intravenously injected HRP@CuS-PEI-Ce6@HA (n = 3). **(c)** The biodistribution of Cu in the main tissues after the intravenous administration of HRP@CuS-PEI-Ce6@HA into tumor-bearing mice (n = 3). **(d)** Photoacoustic imaging in 4T1 tumor-bearing mice treated by HRP@CuS-PEI-Ce6@HA with different lengths of time. **(e)** Thermal images of 4T1 tumors in living mice with 24 h post i.v. injection of PBS and HRP@CuS-PEI-Ce6@HA upon NIR irradiation (808 nm, 0.5 W/cm^2). **(f)** Relative tumor volumes and **(g)** body weight of mice after 7 days of various treatments (PBS, Ce6, HRP@CuS-Ce6@HA + 671 nm, HRP@CPC@HA + 671 nm, CPC@HA + 808 nm + 671 nm and HRP@CPC@HA + 808 nm + 671 nm). **(h)** Representative tumor photographs after 7 days of various treatments: **(i)** PBS, **(ii)** Ce6 + 671 nm, **(iii)** HRP@CuS-Ce6@HA + 671 nm, **(iv)** HRP@CPC@HA + 671 nm, **(v)** CPC@HA + 808 nm + 671 nm, **(vi)** HRP@CPC@HA + 808 nm + 671 nm.

intensity of the signal gradually increased in 24 h. This result suggests that HRP@CPC@HA could accumulate at tumor site effectively due to the active targeting pathway of HA. Furthermore, the thermal images of 4T1 tumor bearing mice were obtained as displayed in Fig. 7e. The tumor areas were treated with 808 nm laser irradiation after 24 h post tail vein injection of HRP@CPC@HA. Compared with control group, the HRP@CPC@HA induced the tumor temperature increases of 19.4 °C under 180 s laser irradiation. This reveals that HRP@CPC@HA could increase local temperature in solid tumor effectively.

Subsequently, tumor suppression of HRP@CPC@HA was investigated in 4T1 tumor-bearing mice. The 4T1 tumor-bearing mice were randomly divided into 6 groups and treated with **i)** PBS, **ii)** Ce6 + 671 nm, **iii)** HRP@CuS-Ce6@HA + 671 nm, **iv)** HRP@CPC@HA + 671 nm, **v)** CPC@HA + 808 nm + 671 nm and **vi)** HRP@CPC@HA + 808 nm + 671 nm respectively. According to the above PA imaging results, the mice were irradiated with laser after 24 h post tail vein injection. After different treatments, the tumor volumes and mouse body weights were peri-odically monitored in all experimental groups (Fig. 7f–g). For mice treated with PBS or free Ce6, the tumor volume exhibits obviously increase and the mice body weight decrease gradually, indicating that PBS or Ce6 alone shows negligible therapeutic effect. For the HRP@CuS-Ce6@HA group with 671 nm laser irradiation, the tumor growth only showed partial suppression, with the relative tumor volume remaining at 3.27. Conversely, HRP@CPC@HA with 671 nm laser irradiation group exhibits more obviously tumor ablation (relative tumor volume 2.76). This indicates that the satellite structure (PEI-Ce6) enables the separation of Ce6 and promotes the diffusion of ROS. To investigate the effect of oxygen in PDT process, 4T1 tumor-bearing mice were treated with HRP@CPC@HA and CPC@HA respectively. Compared with HRP@CPC@HA group, the CPC@HA treated mice exhibits less tumor ablation, indicating that the catalytic decomposition of hydrogen peroxide by HRP and the produced O_2 were crucial to PDT process. Notably, upon 808 nm and 671 nm irradiation simultaneously, the HRP@CPC@HA group achieved complete tumor inhibition. This indicates promising therapeutic efficacy of photothermal and ROS diffusion-enhanced PDT in vivo. Fig. 7h shows the collected tumor pictures after 7 days of various treatments. HRP@CPC@HA group exhibits obviously hypoxic tumor suppression. This suggests ROS diffusion enhanced PDT is an effective strategy for hypoxic tumor therapy.

In addition, the histological evaluation of main organs (heart, liver, spleen, lung, and kidney) slices of mice in each group after antitumor treatment was investigated. The organs were H&E staining for pathological analysis (Fig. 8). The main organs of each treatment group showed relatively normal histological morphology and no obvious

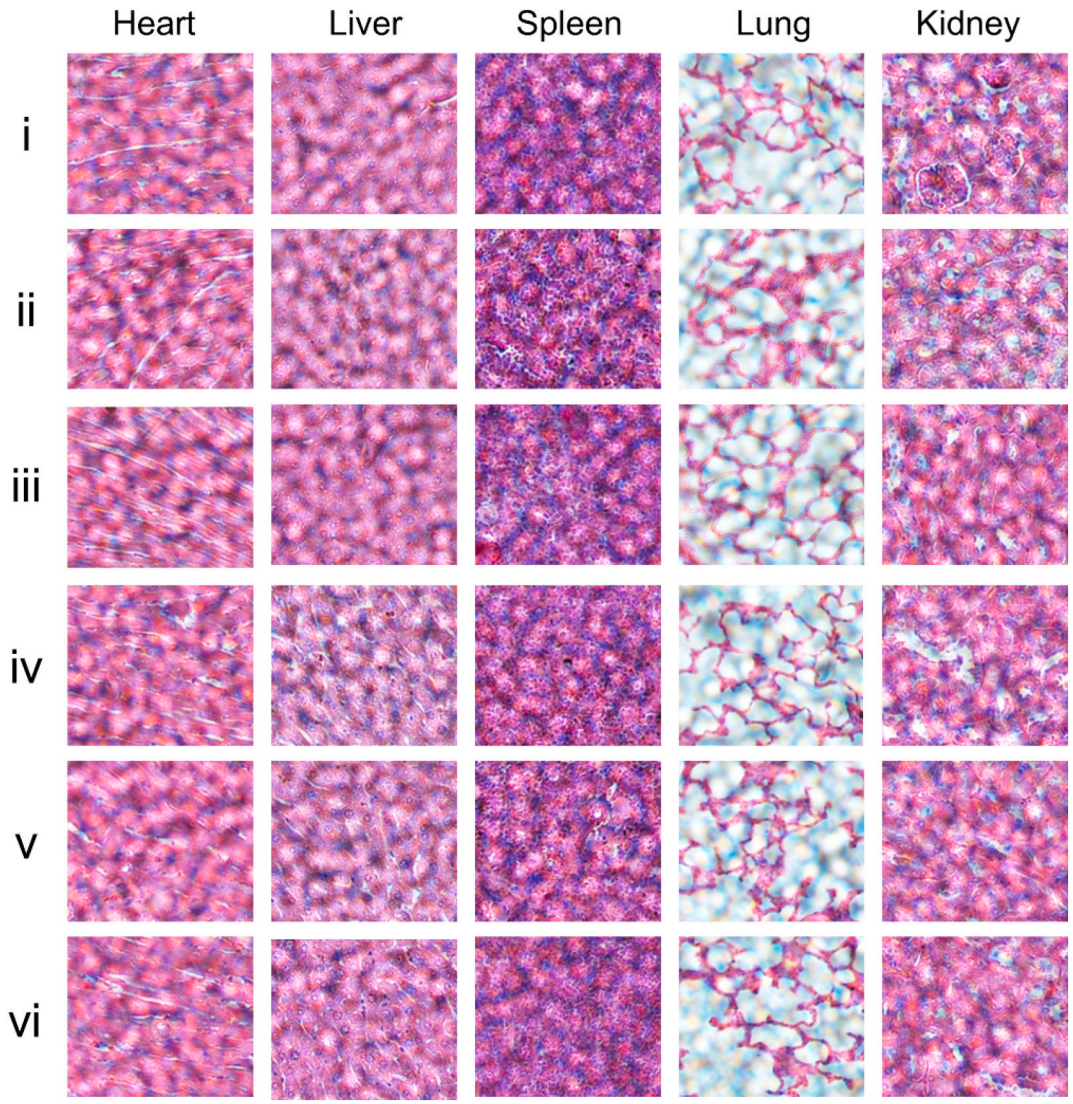

Fig. 8. Tissue sections of major organs (heart, liver, spleen, lung, and kidney) of mice in different treatment groups: **(i)** PBS, **(ii)** Ce6 + 671 nm, **(iii)** HRP@CuS-Ce6@HA + 671 nm, **(iv)** HRP@CPC@HA + 671 nm, **(v)** CPC@HA + 808 nm + 671 nm, **(vi)** HRP@CPC@HA + 808 nm + 671 nm).

pathological abnormality was noticed. This indicated that HRP@CPC@HA exhibited excellent biocompatibility. Taken together, the as-prepared nanoreactor enables ROS diffusion enhanced PDT with precise guidance from PA imaging for efficient and safe hypoxic tumor ablation.

4. Conclusion

In this study, we present novel porous core-satellite nanoreactors (HRP@CPC@HA) for hypoxia tumor therapy via ROS-enhanced phototherapy. The nanoreactors decompose intracellular H_2O_2 by HRP to generate endogenous O_2, increasing O_2 levels on the surface of the nanoreactor via the porous structure of the hollow CuS nanocage. Due to the covalent-linked PEI-Ce6 satellite, Ce6 is uniformly dispersed on the surface of the nanoreactors and avoiding aggregation. With laser irradiation, the generated ROS on the surface of the nanoreactors ensure a larger diffusion range. Meanwhile, the photothermal effect of CuS accelerates the photodynamic process and causes thermal damage to the tumor. In vitro experiments show that HRP@CPC@HA could ablate tumor cells by photodynamic and photothermal effect. Our nanoreactor can accomplish hypoxic tumor inhibition guided by PA imaging. The design of HRP@CPC@HA provides unique strategy of PS delivery, further promoting the application and research of associated nanoreactors.

CRediT authorship contribution statement

Xin Mu: Conceptualization, Methodology, Software, Investigation, Formal analysis, Writing – original draft. **Yulei Chang:** Data curation, Supervision. **Ying Bao:** Visualization, Writing – original draft. **Anni Cui:** Software, Validation. **Xiahua Zhong:** Software, Validation. **Griffin B. Cooper:** Visualization, Writing – review & editing. **Anika Guo:** Investigation, Writing – review & editing. **Guiye Shan:** Conceptualization, Funding acquisition, Resources, Supervision, Writing – review & editing.

Declaration of competing interest

The authors declare that they have no known competing financial interests or personal relationships that could have appeared to influence the work reported in this paper.

Data availability

Data will be made available on request.

Acknowledgments

This work was supported by the National Natural Science Foundation of China (11774048) and the Project from Key Laboratory for UV-Emitting Materials and Technology of Ministry of Education (No. 130028723). Innovative research group project of the National Natural Science Foundation of China, 11774048, Guiye Shan.

References

[1] H. Yang, R. Liu, Y. Xu, L. Qian, Z. Dai, Photosensitizer nanoparticles boost photodynamic therapy for pancreatic cancer treatment, Nanomicro. Lett. 13 (2021) 35, https://doi.org/10.1007/s40820-020-00561-8.

[2] L.P. Zhao, R.R. Zheng, J.Q. Huang, X.Y. Chen, F.A. Deng, Y.B. Liu, C.Y. Huang, X. Y. Yu, H. Cheng, S.Y. Li, Self-delivery photo-immune stimulators for photodynamic sensitized tumor immunotherapy, ACS Nano 14 (2020) 17100–17113, https://doi.org/10.1021/acsnano.0c06765.

[3] F. Li, Y. Du, J. Liu, H. Sun, J. Wang, R. Li, D. Kim, T. Hyeon, D. Ling, Responsive assembly of upconversion nanoparticles for pH-activated and near-infrared-triggered photodynamic therapy of deep tumors, Adv. Mater. 30 (2018) 1802808, https://doi.org/10.1002/adma.201802808.

[4] B.M. Luby, C.D. Walsh, G. Zheng, Advanced photosensitizer activation strategies for smarter photodynamic therapy beacons, Angew. Chem. Int. Ed. 58 (2019) 2558–2569, https://doi.org/10.1002/anie.201805246.

[5] N. Zhang, F. Zhao, Q. Zou, Y. Li, G. Ma, X. Yan, Multitriggered tumor-responsive drug delivery vehicles based on protein and polypeptide coassembly for enhanced photodynamic tumor ablation, Small 12 (2016) 5936–5943, https://doi.org/10.1002/smll.201602339.

[6] Z. Liu, T. Cao, Y. Xue, M. Li, M. Wu, J.W. Engle, Q. He, W. Cai, M. Lan, W. Zhang, Self-amplified photodynamic therapy through the (1) O2 -mediated internalization of photosensitizers from a ppa-bearing block copolymer, Angew. Chem. Int. Ed. 59 (2020) 3711–3717, https://doi.org/10.1002/anie.201914434.

[7] B. Yang, Y. Chen, J. Shi, Reactive oxygen species (ROS)-based nanomedicine, Chem. Rev. 119 (2019) 4881–4985, https://doi.org/10.1021/acs.chemrev.8b00626.

[8] B. Chu, Y. Qu, X. He, Y. Hao, C. Yang, Y. Yang, D. Hu, F. Wang, Z. Qian, ROS-responsive camptothecin prodrug nanoparticles for on-demand drug release and combination of chemotherapy and photodynamic therapy, Adv. Funct. Mater. 30 (2020) 2005918, https://doi.org/10.1002/adfm.202005918.

[9] J. Li, K. Kataoka, Chemo-physical strategies to advance the in vivo functionality of targeted nanomedicine: the next generation, J. Am. Chem. Soc. 143 (2021) 538–559, https://doi.org/10.1021/jacs.0c09029.

[10] N. Lu, Z. Deng, J. Gao, C. Liang, H. Xia, P. Zhang, An osmium-peroxo complex for photoactive therapy of hypoxic tumors, Nat. Commun. 13 (2022) 2245, https://doi.org/10.1038/s41467-022-29969-z.

[11] J. Zhang, Y. Liu, X. Wang, J. Du, K. Song, B. Li, H. Chang, R. Ouyang, Y. Miao, Y. Sun, Y. Li, Nanozyme-incorporated biodegradable bismuth mesoporous radiosensitizer for tumor microenvironment-modulated hypoxic tumor thermoradiotherapy, ACS Appl. Mater. Interfaces 12 (2020) 57768–57781, https://doi.org/10.1021/acsami.0c18853.

[12] Y. Zhang, Y. Liao, Q. Tang, J. Lin, P. Huang, Biomimetic nanoemulsion for synergistic photodynamic-immunotherapy against hypoxic breast tumor, Angew. Chem. Int. Ed. 60 (2021) 10647–10653, https://doi.org/10.1002/anie.202015590.

[13] X. Li, J.F. Lovell, J. Yoon, X. Chen, Clinical development and potential of photothermal and photodynamic therapies for cancer, Nat. Rev. Clin. Oncol. 17 (2020) 657–674, https://doi.org/10.1038/s41571-020-0410-2.

[14] H.S. El-Sawy, A.M. Al-Abd, T.A. Ahmed, K.M. El-Say, V.P. Torchilin, Stimuli-responsive Nano-architecture drug-delivery systems to solid tumor micromilieu: past, present, and future perspectives, ACS Nano 12 (2018) 10636–10664, https://doi.org/10.1021/acsnano.8b06104.

[15] D.B. Cheng, X.H. Zhang, Y.J. Gao, L. Ji, D. Hou, Z. Wang, W. Xu, Z.Y. Qiao, H. Wang, Endogenous reactive oxygen species-triggered morphology transformation for enhanced cooperative interaction with mitochondria, J. Am. Chem. Soc. 141 (2019) 7235–7239, https://doi.org/10.1021/jacs.8b07727.

[16] S. He, S. Lu, S. Liu, T. Li, J. Li, S. Sun, M. Liu, K. Liang, X. Fu, F. Chen, G. Meng, L. Zhang, J. Hai, B. Wang, Spatiotemporally controlled O2 and singlet oxygen self-sufficient nanophotosensitizers enable the in vivo high-yield synthesis of drugs and efficient hypoxic tumor therapy, Chem. Sci. 11 (2020) 8817–8827, https://doi.org/10.1039/d0sc02387f.

[17] X. Huang, J. Wu, M. He, X. Hou, Y. Wang, X. Cai, H. Xin, F. Gao, Y. Chen, Combined cancer chemo-photodynamic and photothermal therapy based on ICG/PDA/TPZ-loaded nanoparticles, Mol. Pharm. 16 (2019) 2172–2183, https://doi.org/10.1021/acs.molpharmaceut.9b00119.

[18] L. Feng, R. Zhao, B. Liu, F. He, S. Gai, Y. Chen, P. Yang, Near-infrared upconversion mesoporous tin oxide bio-photocatalyst for H2O2-activatable O2-generating magnetic targeting synergetic treatment, ACS Appl. Mater. Interfaces 12 (2020) 41047–41061, https://doi.org/10.1021/acsami.0c10685.

[19] K. Lu, C. He, W. Lin, Nanoscale metal-organic framework for highly effective photodynamic therapy of resistant head and neck cancer, J. Am. Chem. Soc. 136 (2014) 16712–16715, https://doi.org/10.1021/ja508679h.

[20] J.N. Liu, W. Bu, J. Shi, Chemical design and synthesis of functionalized probes for imaging and treating tumor hypoxia, Chem. Rev. 117 (2017) 6160–6224, https://doi.org/10.1021/acs.chemrev.6b00525.

[21] T. Shen, X. Hu, Y. Liu, Y. Zhang, K. Chen, S. Xie, G. Ke, G. Song, X.B. Zhang, Specific Core-satellite nanocarriers for enhanced intracellular ROS generation and synergistic photodynamic therapy, ACS Appl. Mater. Interfaces 12 (2020) 5403–5412, https://doi.org/10.1021/acsami.9b16934.

[22] Y. Li, G. Liu, J. Ma, J. Lin, H. Lin, G. Su, D. Chen, S. Ye, X. Chen, X. Zhu, Z. Hou, Chemotherapeutic drug-photothermal agent co-self-assembling nanoparticles for near-infrared fluorescence and photoacoustic dual-modal imaging-guided chemo-photothermal synergistic therapy, J. Control. Release 258 (2017) 95–107, https://doi.org/10.1016/j.jconrel.2017.05.011.

[23] M. Li, X. Sun, N. Zhang, W. Wang, Y. Yang, H. Jia, W. Liu, NIR-activated polydopamine-coated carrier-free "Nanobomb" for in situ on-demand drug release, Adv. Sci. 5 (2018) 1800155, https://doi.org/10.1002/advs.201800155.

[24] D. Wang, H. Wu, G. Yang, C. Qian, L. Gu, H. Wang, W. Zhou, J. Liu, Y. Wu, X. Zhang, Z. Guo, H. Chen, D. Jana, Y. Zhao, Metal-organic framework derived multicomponent nanoagent as a reactive oxygen species amplifier for enhanced photodynamic therapy, ACS Nano 14 (2020) 13500–13511, https://doi.org/10.1021/acsnano.0c05499.

[25] W. Zuo, D. Chen, Z. Fan, L. Chen, Z. Zhu, Q. Zhu, X. Zhu, Design of light/ROS cascade-responsive tumor-recognizing nanotheranostics for spatiotemporally controlled drug release in locoregional photo-chemotherapy, Acta Biomater. 111 (2020) 327–340, https://doi.org/10.1016/j.actbio.2020.04.052.

[26] J. Qi, Y. Fang, R.T.K. Kwok, X. Zhang, X. Hu, J.W.Y. Lam, D. Ding, B.Z. Tang, Highly stable organic small molecular nanoparticles as an advanced and biocompatible phototheranostic agent of tumor in living mice, ACS Nano 11 (2017) 7177–7188, https://doi.org/10.1021/acsnano.7b03062.

[27] Y. Li, J. Lin, P. Wang, Q. Luo, H. Lin, Y. Zhang, Z. Hou, J. Liu, X. Liu, Tumor microenvironment responsive shape-reversal self-targeting virus-inspired

nanodrug for imaging-guided near-infrared-II photothermal chemotherapy, ACS Nano 13 (2019) 12912–12928, https://doi.org/10.1021/acsnano.9b05425.
[28] C. Li, G. Chen, Y. Zhang, F. Wu, Q. Wang, Advanced fluorescence imaging Technology in the Near-Infrared-II window for biomedical applications, J. Am. Chem. Soc. 142 (2020) 14789–14804, https://doi.org/10.1021/jacs.0c07022.
[29] F. Yu, M. Zhu, N. Li, M. Ao, Y. Li, M. Zhong, Q. Yuan, H. Chen, Z. Fan, Y. Wang, Z. Hou, Z. Qi, Y. Shen, X.D. Chen, Imaging-guided synergistic targeting-promoted photo-chemotherapy against cancers by methotrexate-conjugated hyaluronic acid nanoparticles, Chem. Eng. J. 380 (2020), 122426, https://doi.org/10.1016/j.cej.2019.122426.
[30] X. Jia, J. He, L. Shen, J. Chen, Z. Wei, X. Qin, D. Niu, Y. Li, J. Shi, Gradient redox-responsive and two-stage rocket-mimetic drug delivery system for improved tumor accumulation and safe chemotherapy, Nano Lett. 19 (2019) 8690–8700, https://doi.org/10.1021/acs.nanolett.9b03340.
[31] G. Li, S. Yuan, D. Deng, T. Ou, Y. Li, R. Sun, Q. Lei, X. Wang, W. Shen, Y. Cheng, Z. Liu, S. Wu, Fluorinated polyethylenimine to enable transmucosal delivery of photosensitizer-conjugated catalase for photodynamic therapy of orthotopic bladder tumors postintravesical instillation, Adv. Funct. Mater. 29 (2019) 1901932, https://doi.org/10.1002/adfm.201901932.
[32] H. Shi, Y. Sun, R. Yan, S. Liu, L. Zhu, S. Liu, Y. Feng, P. Wang, J. He, Z. Zhou, D. Ye, Magnetic semiconductor gd-doping CuS nanoparticles as activatable nanoprobes for bimodal imaging and targeted photothermal therapy of gastric tumors, Nano Lett. 19 (2019) 937–947, https://doi.org/10.1021/acs.nanolett.8b04179.
[33] R. Zhao, X. Sun, J. Sun, L. Wang, J. Han, Polypyrrole-modified CuS nanoprisms for efficient near-infrared photothermal therapy, RSC Adv. 7 (2017) 10143–10149, https://doi.org/10.1039/c6ra28228h.
[34] D. Gao, Z. Sheng, Y. Liu, D. Hu, J. Zhang, X. Zhang, H. Zheng, Z. Yuan, Protein-modified CuS nanotriangles: a potential multimodal nanoplatform for in vivo tumor Photoacoustic/Magnetic resonance dual-modal imaging, Adv. Healthc. Mater. 6 (2017) 1601094, https://doi.org/10.1002/adhm.201601094.
[35] H. Zhu, J. Wang, D. Wu, Fast synthesis, formation mechanism, and control of shell thickness of CuS hollow spheres, Inorg. Chem. 48 (2009) 7099–7104, https://doi.org/10.1021/ic900201p.